

See discussions, stats, and author profiles for this publication at: <https://www.researchgate.net/publication/323636673>

A fast approach for large-scale Sky View Factor estimation using street view images

Article in *Building and Environment* · March 2018

DOI: 10.1016/j.buildenv.2018.03.009

CITATION

1

READS

168

4 authors, including:



Liyue Zeng

Chongqing University

6 PUBLICATIONS **5 CITATIONS**

[SEE PROFILE](#)



Jun lu

Chongqing University

37 PUBLICATIONS **56 CITATIONS**

[SEE PROFILE](#)

Some of the authors of this publication are also working on these related projects:



national fundamental item [View project](#)



A fast approach for large-scale Sky View Factor estimation using street view images

Liyue Zeng, Jun Lu*, Wuyan Li, Yongcai Li

Key Laboratory of the Three Gorges Reservoir Region's Eco-Environment, Ministry of Education, Chongqing University, Chongqing, 400045, China

ARTICLE INFO

Keywords:

Sky view factor
Street canyon
Sky detection
Big data
Fish-eye

ABSTRACT

Sky View Factor (SVF) is one of the most useful urban spatial indicators for radiation and thermal environmental assessment. Estimating SVF with circular fish-eye photos is straightforward and convenient and can account for obstruction of vegetation and other urban infrastructures. But for a large area with many points of interest, processing fish-eye photos is labor intensive. This paper presents a workflow of estimating SVF with large amounts of street view images obtained at sampling points along city road network at the height of about 2 m. To automatically estimate SVF with street view images, a batch processing sky region detection and SVF calculation tool was developed with the Python programming language and OpenCV. The tool can deal with various outdoor weather conditions, and the performance of sky region segmentation and SVF calculation was validated with photos taken with a fish-eye lens. The method shows reliable estimations and preferable speed, with about 1.5 s for a 1000 × 500 px image and 0.08 s for a 200 × 100 px image. The proposed workflow was further applied to estimate the SVF distributions in the downtown centers of four densely populated Chinese cities.

1. Introduction

Urban morphology has a significant influence on the micro-climate of cities, and numerous studies have attempted to reveal the relationship between urban morphology and the outdoor thermal condition. Height to width ratio (H/W) and Sky View Factor (SVF) are among the most discussed urban morphological parameters [1–13]. Sky View Factor (SVF) refers to the ratio of the radiation received by a planar surface to the radiation emitted by the entire hemispheric environment [14,15]. SVF is typically represented by a dimensionless value between 0 and 1, where 0 indicates the sky is completely obstructed by obstacles and 1 indicates there are no obstructions at all [16]. SVF is a widely used parameter to study Urban Heat Island (UHI) effect [17], urban energy balance [18,19], and urban surface temperature [12,20], and controlling SVF can prevent high temperatures in urban street canyons [21]. Oke [22] suggested a negative linear correlation between the maximum heat island intensity and SVF. Unger [23] reported a strong negative relationship between areal averages of SVF and UHI through mobile measurement within a large sample area. Svensson et al. [10] also reported a fairly strong relationship between nighttime street-level air temperature and SVF.

In outdoor thermal comfort studies, SVF is found to be closely related to physiologically equivalent temperature (PET) [6] and mean radiant temperature (MRT) [24,25]. Lin et al. [6] performed a 10-year

PET prediction for a hot summer mild winter climate and found high SVF locations are uncomfortable in summer. Among all their studied sites, a SVF of 0.129 has the longest annual thermal comfort period. Holst and Mayer [25] reported a linear relationship between the MRT and SVF in street canyons. Because these thermal parameters also significantly affect the visiting frequency of public spaces [5,26], identifying SVF distribution pattern would be valuable for urban planning and renovation. However, in spite of the abundant studies concerning SVF, previous studies have revealed the need for investigations into a larger number of survey sites or the entire city to obtain the effect of SVF [27].

SVF can be estimated with 3D city model-based methods [28,29], GPS method [30–32], or the fish-eye photo-based methods [16]. Urban 3D model-based methods can estimate continuous SVF distribution in a large area with a short calculating time. A few tools have been developed for this purpose, either standalone tools or GIS software plugins. For example, plugins in ArcView have been developed for estimating SVF using vector-based digital maps that contains building shape information [23,33]. The SkyHelios tool developed by Matzarakis et al. [34,35] can also generate continuous SVF map using Digital Surface Models (DSMs). Furthermore, a few multi-functional urban climatic software packages are able to perform SVF calculations. The SOLWEIG (Solar and LongWave Environmental Irradiance Geometry model), which is a component of the Urban Multi-scale Environmental Predictor

* Corresponding author.

E-mail addresses: soriyoshi91@163.com (L. Zeng), 20131702056@cqu.edu.cn (J. Lu), wuyanlee@foxmail.com (W. Li), yongcail@yahoo.com (Y. Li).

(UMEP), an integrated urban environmental assessment tool developed by Grimmond et al. [36] also enables SVF calculation as well as MRT modeling. Some other micro-climatic software also has the SVF calculation function, such as ENVI-met and HURES [37], and most of them are based on 3D vectored processing. A common limitation of the above methods is that vegetation and obstacles other than buildings are rarely included in the available 3D database. However, in real urban environment, other intra-urban obstacles especially the vegetation would also affect SVF estimation [38]. This limitation can be overcome by highly detailed 3D databases. For example, a recently developed SVF calculation tool named SVFEngine [39] enables accurate estimation of SVF using highly detailed 3D urban model obtained with oblique airborne photogrammetry. Although the result can accurately reveal the current urban canopy status with even vegetation into consideration, the required data size could reach several gigabytes for the city scale. Overall, although 3D city model-based methods are fairly efficient once the 3D obstacle database is available, these data sources are not widely available.

Another kind of method, namely the GPS method, estimates SVF through multiple variable regression or Artificial Neural Network (ANN) regression that relate SVF to on-site satellite visibility and signal strength data [30–32]. This method enables real time estimation and works fairly well in urban areas ($r = 0.65\text{--}0.67$), while in rural areas the performance decreases ($r = 0.46\text{--}0.51$), which might be due to the effect of trees.

A number of studies estimate SVF using fish-eye photos [16,40], which can be obtained by taking photos upwards the zenith with a circular fish-eye lens at the ground level. With circular fish-eye photos, the sky region and the obstructed region can be delineated with image processing software. But the process is usually performed manually, one image at a time. Once the sky segmentation process is finished, there are different ways to calculate SVF with circular fish-eye photos. The Rayman software [41] is a micro-scale model that enables estimating SVF, sunshine duration, shadow and thermal indices. It calculates SVF using either 3D building and plant models or fish-eye photos. For the fish-eye photograph calculation mode, the sky region segmentation can be achieved by free-hand drawing or by RGB threshold-based cropping. However, unsupervised automated batch processing of fish-eye photos is not possible with this software [24]. There are three main obstacles in applying this method to large scale SVF assessment: very time-consuming manual image processing, limited surveying opportunities, and ideal overcast sky conditions to ensure sky identification accuracy [28]. SKYVIEW [42] is an application developed for SVF-targeted automated image processing, but the limitation is that the process needs redefining parameters manually and the performance largely relies on perfect overcast weather condition.

Recently, with the development of big data applications, it is realized that street view photos have great potential in urban environmental studies, since the street view images can cover most of the urban areas in the world and provides unprecedented survey opportunity.

Street view images, especially Google Street View images are more and more frequently used for scientific purposes. The study by Carrasco-Hernandez et al. [43] is the first that used Google Street View photos for SVF and solar radiation estimation. Liang et al. [44] carried out a pilot study on large-scale SVF estimation using Google Street View and an open source CNN tool named SegNet [45], which aims at identifying different kinds of components in outdoor and indoor images. Another machine learning technique Support Vector Machine (SVM) is reported to be used in street view photo-based street visual enclosure estimation [46]. These studies demonstrate the possibility of unsupervised automated large-scale SVF estimation, and the processing time for a city-scale estimation could be just a few hours if a GPU calculation platform is available. However, the open source CNN tool still took tens of hours for a city-scale estimation on a common CPU platform. It is beneficial to reduce the required time and this should be possible since the recognitions with SegNet are performed for many types of outdoor components while only the sky is needed.

In this paper, we present an efficient workflow for estimating SVF at a large scale using street view photographs. Static panorama images for a large number of sampling points based on road net database can be accessed through API requests. Then an automatic batch processing sky region detection and SVF calculation tool is developed with the Python programming language. The tool can deal with various outdoor weather conditions, and the performance of sky region segmentation and SVF calculation was validated with photos taken with a Nikon FC-E9 fish-eye lens. The method shows reliable estimations and preferable speed. The proposed workflow was further applied to estimate the SVF distributions in the downtown centers of four densely populated Chinese cities within different climate zones.

2. Methodology

2.1. Street view map acquisition

In recent years, Google Street Map is more and more frequently used for scientific purposes [44,46,47]. It covers many cities around the world, but some regions such as China are not covered. However, there are a few alternative map providers, such as Baidu [48] and Tencent [49]. Static panorama images can be accessed via APIs given the field of view (FOV), heading, pitch, image size, longitude and latitude location or panorama ID, etc. More information on keys and values for street view image acquisition can be found through the Baidu website [48]. Baidu provides static panorama images with a maximum FOV of 360° in the horizontal direction and an FOV of 180° in the vertical direction. Fig. 1 shows the example of Baidu Street Map coverage for Shanghai, China (in the light blue mask), and a sample street view image with the size of 600×300 pixels. The retrieved panorama images can be directly used for the sky region detection process described in the following section. However, for providers with a maximum FOV of less than 360° , a panorama stitching process with a set of rectilinear street

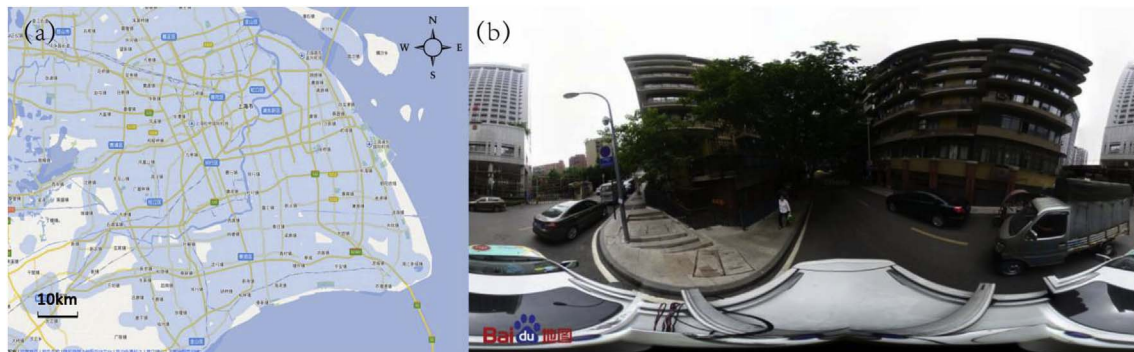


Fig. 1. (a) Coverage of panorama image in Baidu Street View, Shanghai, China; (b) an example of the retrieved panorama (fov = 360×180) [48].

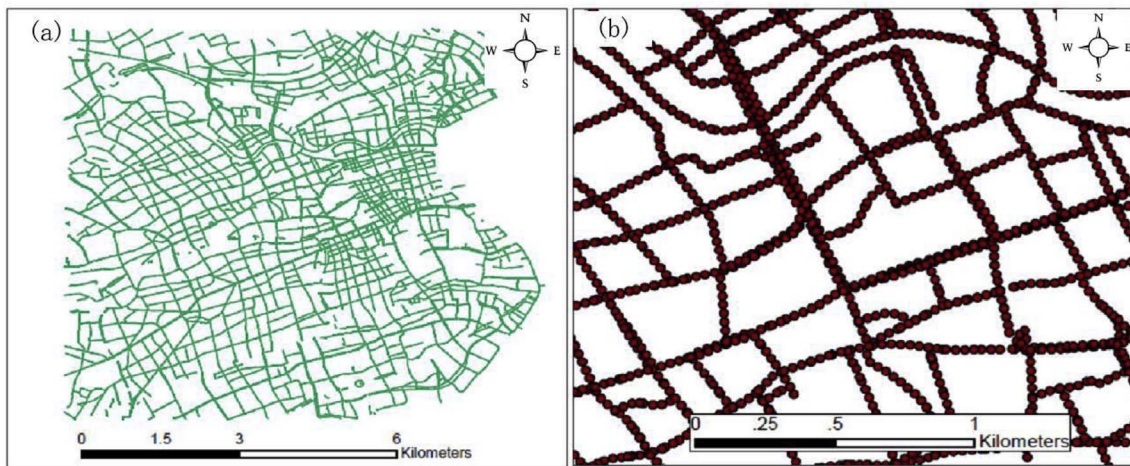


Fig. 2. (a) Road net of the central area of Shanghai, China; (b) a closer look at the point cloud obtained by sampling along the streets.

view images is needed [43]. The panorama stitching process can be achieved with tools like Hugin [50] or by coordination transformation [44,51]. Since the panorama reconstruction is not needed in our study, we do not further elaborate on this. More detailed information can be found in Refs. [39,43,51].

Fig. 2 shows the road net of the central area of Shanghai, China, and a close look at the detail sampling points of a small area. The point cloud is obtained by sampling over the target road net with a spacing of $0.0003\text{--}0.0004^\circ$ (which equals about 33.3–44.4 m). For each of the sampling point, a static panorama image was accessed through API requests.

2.2. Sky region detection

The focus of this section lies in the sky region segmentation, which is the most time-consuming procedure in fish-eye photo-based SVF estimation. The sky segmentation process is needed in many applications such as outdoor environment assessment [46], autonomous navigation [52] and image haze removal [53]. Machine learning methods such as CNN and SVM provide fair accuracy, but they require a large number of training samples, and ready-to-use CNN projects [54] may take spare time to segment images into many components while only the sky and non-sky regions are needed. The straight forward sky region detection methods that do not require training samples either cannot deal with occasions where electric wires split the sky [52] or when the upper part of the image is not smooth overcast sky [53]. If street view images were to be used for accurate estimate SVF, difficult situations such as blue sky with plenty of white clouds and street canyon mostly covered with tree crowns should be considered.

Aiming at enabling fast estimation of SVF in a large scale with a huge amount of sampling points, we present a tool based on the cross-platform open source computer vision library OpenCV [55] to automatically acquire the sky region and estimate the SVF with street view panoramas. The overall procedure is depicted in Fig. 3.

The input image is a static panorama image with 360° FOV in the

horizontal direction and 180° FOV in the vertical direction. The image size is adjustable depending on the API requests, but the maximum image size accessible through Baidu API is 1000×1000 pixels (px). It should be noted that smaller image size can significantly reduce processing time but too small image size may decrease estimation accuracy. In the Methodology section, the image size of 600×300 px is used, while an image size sensitivity test is performed in the Discussion section.

First, the input images are classified into two scenarios: images with open sky in the upper region and images with large tree crown shading the sky. The reason for such classification is that we found these two types of photos cannot be well processed with the same algorithm due to different characters. To classify input images, the very first step is to perform an edge detection, which aims at identifying the points in an image at which there are sudden gradient changes. Sky regions are usually unlikely to have abrupt changes in brightness or color, except when there are many clouds. A preliminary sky region can be obtained assuming the regions without edges to be the sky. Edge detections can be achieved with various edge detection algorithms in OpenCV as well as other programming platforms. OpenCV provides a few edge detection methods, and in this work the Canny Edge Detection [56] method is used. By adjusting the Canny Detection parameters, the edges of the clouds in the upper region of the sky can be mostly filtered. Since the region in the lower half of the image is the ground, it is eliminated to accelerate image processing. The 600×300 px image is then presented as a 600×150 matrix with “0” representing non-edge pixels and “1” representing the edge pixels. As an example, Fig. 4 shows the edge detection results for images with and without large tree crown region. Then the images were classified into two types (with open sky in the upper region and images with large tree crown shading the sky) according to whether the proportion of edge pixels (in white color) in the image top area exceeds a threshold (0.1 is used). The images will be classified into the tree crown group if the proportion of edge pixels exceeds the threshold. Otherwise, the images will be identified as having a clear sky in the upper region.

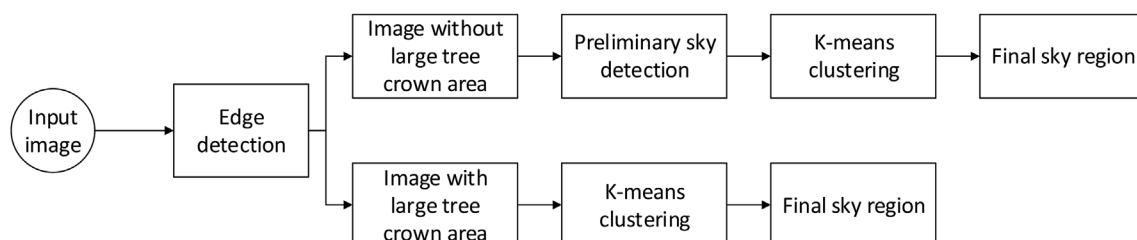


Fig. 3. Flow chart for the skyline delineation and SVF calculation process.

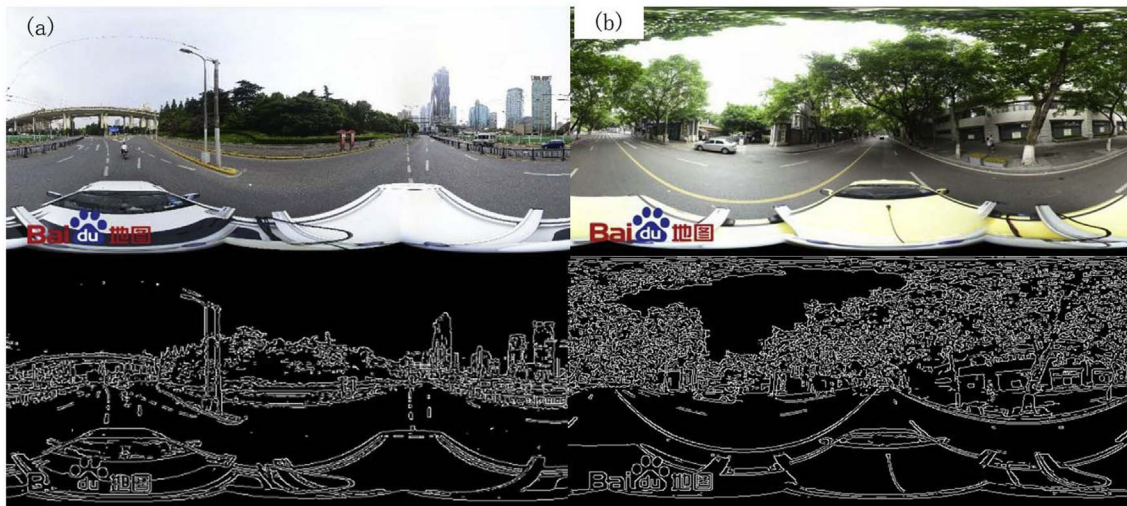


Fig. 4. Street view image samples and edge detection results for images (a) with open sky in the upper region and (b) with large tree crown shading the sky.

2.2.1. Images with open sky in the upper region

For images with open sky in the upper region (Fig. 5(1a–1d)), the preliminary sky region detection involves the process of counting from the topmost pixel (labeled as “0”, black colored) to the first edge pixel (labeled as “1”, white colored), as shown in Fig. 5(1b). This process resembles that proposed by Laugrunthip et al. [57] and used by Middel et al. [51]. But as stated by the authors, the method does not apply to scenarios where many small bright sky areas exist among the tree leaves and branches. Moreover, this preliminary procedure can only detect part of the sky when overhanging obstacles such as electric wires and street light poles exist in the street canyon. In order to fix this, K-means clustering [58], which is an unsupervised learning algorithm that aims at partitioning the image into K clusters according to feature similarity was performed, as shown in Fig. 5(1c). In our work, the number of clusters is chosen to be 12 after a few tests. Next, the clusters that mostly (> 30% of all pixels in the cluster) lie within the preliminary sky region (Fig. 5(1a)) are determined to be sky sub-regions.

Afterwards, for each sub-region, small individual parts are removed, because these parts are usually windows or light-colored walls misclassified into the sky region clusters. Finally, the sky region (Fig. 5(1d)) is obtained by adding up all the sub-regions.

2.2.2. Images with large tree crown shading the sky

When the upper part of the image is covered by tree crowns, the procedure of finding a preliminary sky region by searching from top of the image is not suitable since the top part could be full of edges, as shown in Fig. 4. The first step is performing K-means clustering that divides the image into several clusters according to feature similarity. Afterwards, identifications of the clusters that belong to the sky were needed. To make that possible, the original image was transferred into HLS color space, which includes three feature values: hue, lightness, and saturation. Compared to RGB color space, the HLS color space describes an image more similarly to the perception of a human. The hue H (0° – 360°) describes which color it is, the saturation S (0–1)

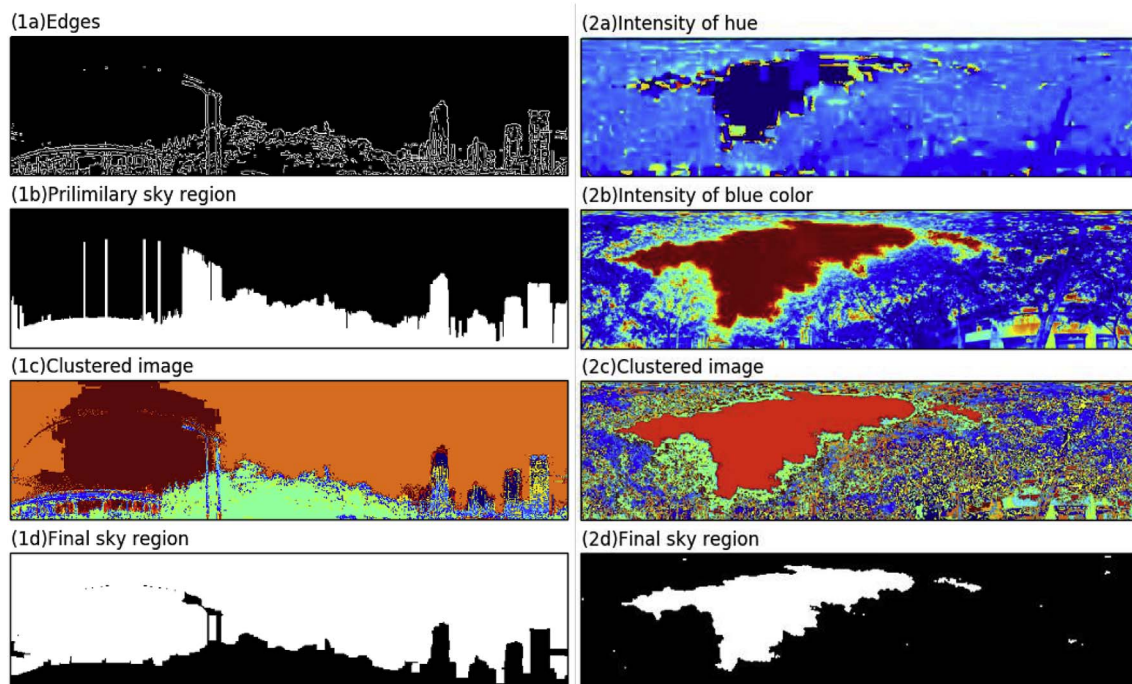


Fig. 5. Sky region detection for different street view scenarios (1a–d) Images with open sky in the upper region; (2a–d) Images with large tree crown shading the sky.

describes the purity of that color, and the lightness L (0–1) describes the brightness of the color. As an example, Fig. 5(2a) depicts the HLS Hue value of an image; Fig. 5(2b) depicts the RGB Blue value, Fig. 5(2c) depicts the K-means clustered image with different colors representing different clusters. Additionally, an important feature of the sky is that the RGB components are very close to each other. The sky regions were determined based on the following features:

$$\begin{aligned} & H \geq 0.35 \\ & \cup L \geq 0.95 \\ \text{Sky}_{\text{pre}} = & \cup (S \leq 0.005 \cap B \geq 0.9B_{\text{max}}) \\ & \cup (S \leq 0.03 \cap B \geq 0.9B_{\text{max}}) \\ & \cup (B \geq 0.95B_{\text{max}} \cap |B - R| < 0.02) \end{aligned} \quad (1)$$

where H , L , S are the normalized hue, lightness, and saturation value, respectively; B , R are the normalized blue and red intensity, respectively; B_{max} is the maximum blue intensity within all the pixels in an image.

For each cluster in the image, if 40% of the pixels in the cluster meet the Sky_{pre} definition, the cluster is determined as a sky region. The final sky region (Fig. 5(2d)) is obtained by adding up all the sub-regions.

2.3. SVF calculation

There are different methods to calculate SVF with fish-eye images. Steyn introduced a method to estimate SVF with circular fish-eye images which are divided into N concentric annuli [59]. Johnson et al. [14] proposed a little modification to the Steyn method, which approximated $\sin[\pi/(2n)]$ by $\pi/(2n)$, as shown in Equation (2). However, the difference induced by the approximation is reported to be less than 0.03% for 40 annuli. Chapman et al. developed a similar equation, as shown in Equation (3) [42], which is used for SVF calculation in this study.

$$\text{SVF} = \frac{1}{2\pi} \sin \frac{\pi}{2n} \sum_{i=1}^n \sin \left(\frac{\pi(2i-1)}{2n} \right) \left(\frac{p_i}{t_i} \right) \quad (2)$$

$$\text{SVF} = \frac{\pi}{2n} \sum_{i=1}^n \sin \left(\frac{\pi(2i-1)}{2n} \right) \left(\frac{p_i}{t_i} \right) \quad (3)$$

where p_i/t_i is the ratio between the number of sky pixels to the total number of pixels in the annulus i .

The acquired static panorama images are rectangular images in equidistant projection. Since the SVF calculation is based on azimuthal images with the equisolid angular projection, we first transferred the images into equisolid projections. Fig. 6 shows the schematic for

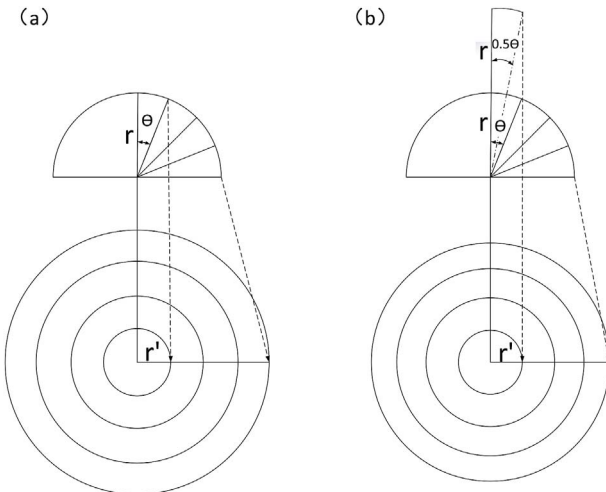


Fig. 6. Schematic of different projections for the skydome: (a) equidistant fish-eye projection; (b) equisolid angular fish-eye projection.

equidistant projection and equisolid angular projection. For equisolid angular projection, the relationship between the radius, the skydome radius and the zenith angle can be expressed as:

$$r' = 2r \sin \left(\frac{\theta}{2} \right) \quad (4)$$

where r' is the radius of the projected image, θ is the azimuth angle, r is the skydome radius.

For equidistant projection, the radius can be calculated as:

$$r' = r \cdot \theta \quad (5)$$

The rectangular images could be transferred into polar coordinate for displaying purpose. But in the calculation process, the images were re-projected from equidistant projection to equisolid angular projection only in the y-axis, since the proportion of sky pixels in each row of rectangular images should be equal to that of the corresponding transformed circular images. So transforming an equidistant projection image with the radius R (identical to a rectangular image with R rows) to an equisolid angular projection with the same radius R can follow Equation (6).

$$P_{a(i)} = P_{d(j)} \quad (6)$$

$$j = \left\lceil R \cdot \left(2 \arcsin \left(\frac{i}{R/\sin(\pi/4)} \right) \right) / \frac{\pi}{2} \right\rceil \quad (7)$$

where $P_{a(i)}$ is the pixel at the i_{th} row of the equisolid angular projection image, $P_{d(j)}$ is the pixel at the j_{th} row of the equidistant projection image.

An example of a processed image transformed from equidistant projection to equisolid angular projection is shown in Fig. 7.

3. Results and discussion

In this section, firstly, an evaluation of the performance of this method is carried out considering the difference between SVF estimations with street view images and those with on-site fish-eye photos. Then the performance of the method for some difficult conditions is discussed and compared to the performance of SegNet. Moreover, the effect of image size on estimation result and processing speed has been evaluated. The method was further used to estimate the SVF distributions in the downtown centers of several densely populated cities within different climate zones in China.

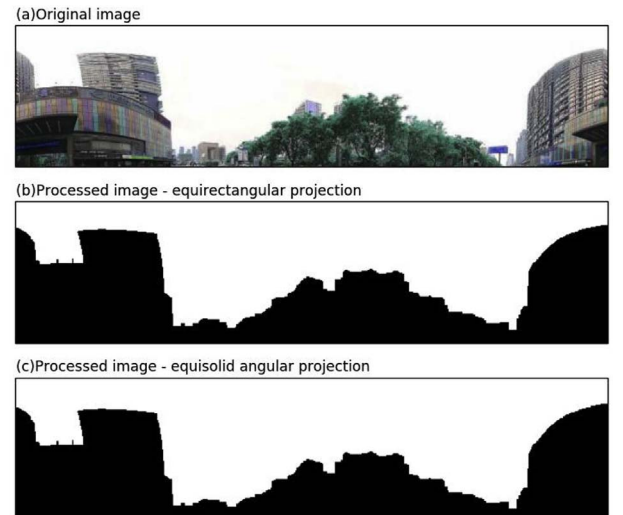


Fig. 7. An example of processed image with different projection methods.

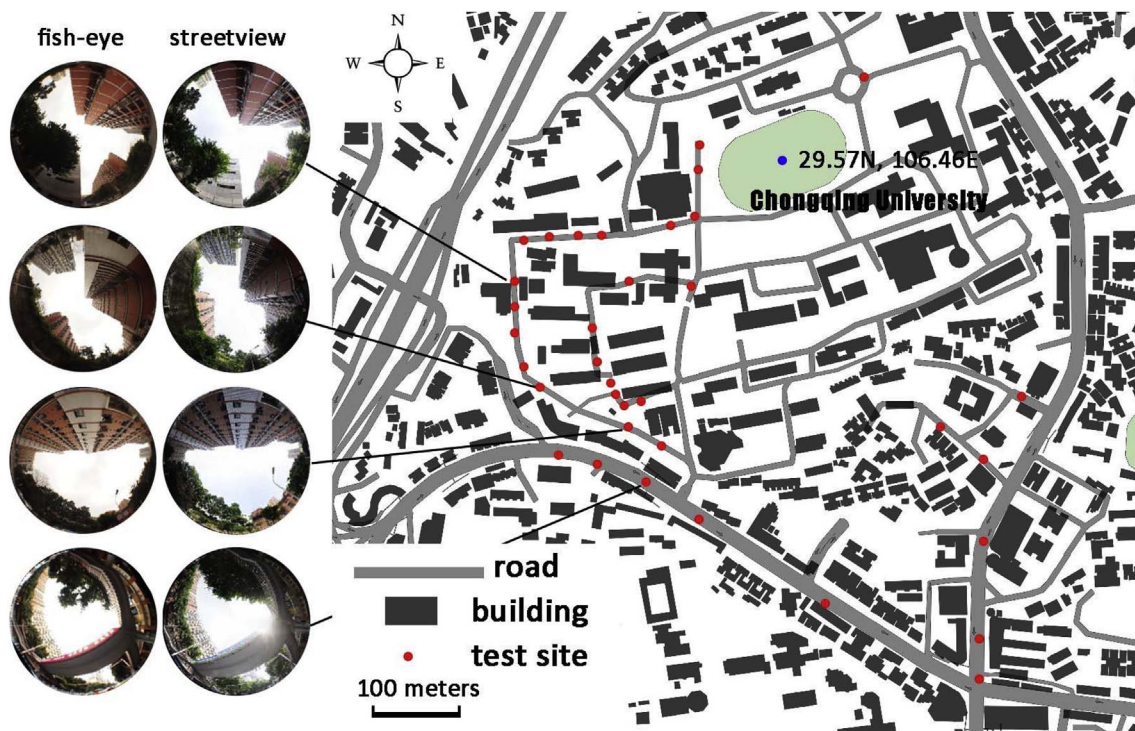


Fig. 8. Map of the study site and positions of the points at which the SVF values are compared between fish-eye photos and street view panoramas.

3.1. Evaluation of the method

3.1.1. Comparison with fish-eye photographs

In order to test the validity of this algorithm, the SVF estimations with the developed method are compared with the estimations from manual sky detection of both street view images and on-site fish-eye photographs. The field experiment was carried out in the campus of Chongqing University, and a total of 35 points were compared, as shown in Fig. 8. The photos were taken with a digital camera (Olympus EM-5) with a fish-eye lens converter (Nikon FC-E9) mounted on a 12–50 mm lens. The FOV of the lens is about 180° at the focal length of 15 mm (30 mm for 35 mm equivalent focal length). These fish-eye photographs were taken as near to the spot of street view image as possible. All photos were taken at about 2 m above ground, since the streetview photos are taken at about 2 m above ground as cameras are installed about 1 m above the vehicle. It should be noted that this height is slightly different from the normally used 1.5 m in outdoor thermal comfort studies. This difference is neglected here, but if the method is to be used to study pedestrian height thermal comfort, further adjustments in the SVF values could be made prior to application.

The comparison of SVF estimations with the three methods (automatic processing of streetview images, manual sky detection of streetview images, and automatic processing of on-site fish-eye photos) are shown in Fig. 9. An RMSE of 0.052 and an R^2 of 0.926 were found between the manual and automatic processed results for streetview images, as shown in Fig. 9(a). And An RMSE of 0.071 and an R^2 of 0.827 were found between the manual and automatic processed results for streetview images, as shown in Fig. 9(b). The slightly larger difference revealed in Fig. 9(b) could be due to the difference between leaf status in different times at which the fish-eye photos/street view photos were taken. Overall, these results suggest the method developed in this paper provides fair SVF estimations. However, since most of the street view images are captured on the roads, SVF in open spaces or near the buildings could be unavailable. In these cases, an on-site campaign is needed to capture photos or videos before the automatic SVF estimation method can be applied.

It should be noted that the estimations can be different with

different SVF calculation algorithms and software. For example, for some algorithms, not all of the pixels in the fish-eye images have the same influence upon SVF calculation, while others might simply calculate the ratio of sky region pixels. A detailed comparison of different methods can be found in Ref. [51]. As for the processing time, the tests were run on a machine with Xeon CPU (E5-2670). The total processing time from sky region segmentation to SVF calculation would take about 0.5–0.6 s for a 600×300 px image, and about 1.5 s for a 1000×500 px image. A previous study [46] took two days to classify a total of 3592 Google Street View images with the size of 1664×832 using an SVM machine learning algorithm, and the processing time for each image is about 20 s to 2 min. Another study using SegNet [44], reported classifying 11,709 1024×1024 panoramas taking about 30 h (10 s per image) with 2 Xeon processors (E5-2630) and 3 h with an NVIDIA Quadro K4200 graphics card. The method used in this paper can reach a preferable speed (at least 5x speed compared to SegNet for a similar image size) on a similar CPU platform. It is promising to be used in real-time SVF survey on a mobile platform with fair accuracy and acceptable speed.

3.1.2. Performance for different sky condition and image quality

In previous attempts [42] to automate the SVF estimation process, an “ideal” homogenous overcast weather condition is required. However, street view images are taken under different weather conditions, and a number of them are taken on fine or cloudy weather days that exhibit various sky features. Fig. 10 shows examples for sky region detection results for different difficult situations: with blue sky and clouds (Fig. 10(a)), with overhanging bridges (Fig. 10(b)), and with overexposed photos (Fig. 10(c)). The results are also compared with that detected with SegNet. It can be seen that the detection is successful in all the conditions except when the photo quality is severely damaged by overexposure, when SegNet also fails in detecting the buildings on the right side of the image (Fig. 10(c)). But since overexposed images take a very small percentage of all the images in a large area, this should have little effect in large-scale SVF estimation.

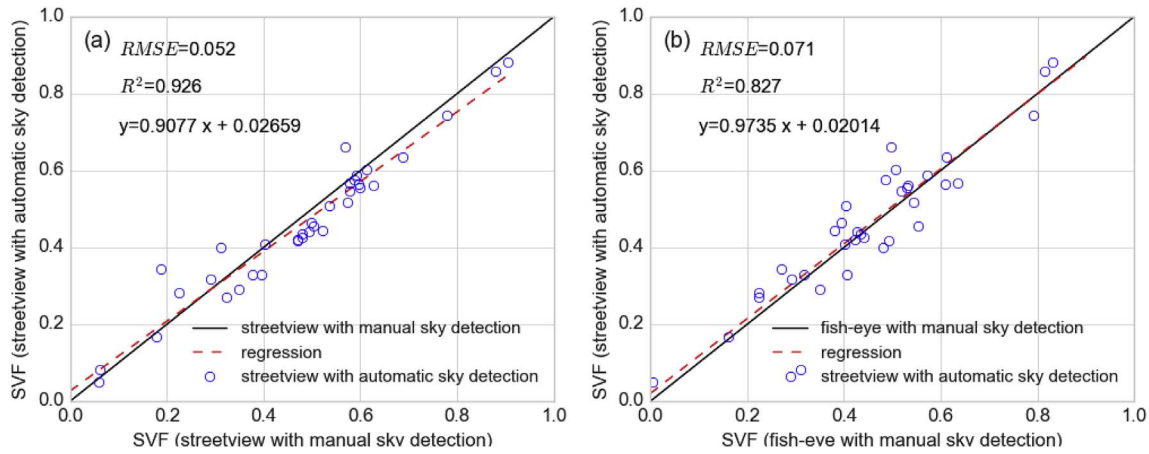


Fig. 9. (a) Comparison of SVF estimated from automatic processing of streetview images and those estimated from manual sky detection of street view images; (b) Comparison of SVF estimated from automatic processing of streetview images and those estimated from manual sky detection of fish-eye photographs.

3.1.3. The effect of image size

Image size also affects estimation accuracy and speed, because larger sizes may have higher image quality but require far more processing time. This is important especially for fast SVF estimation on a large scale. To test the effect of image size on the SVF estimation results, we compared 7 image sizes (1000×500 px, 800×400 px, 600×300 px, 500×250 px, 400×200 px, 300×150 px, 200×100 px) using 100 randomly selected images that cover most of the possible situations: mostly tree-covered, open wide canyons with low buildings, narrow canyons with tall buildings, overexposure photographs, open blue sky with white clouds. The size of 1000×500 px is set as a standard size with the best image quality. Fig. 11 shows the comparisons of SVF estimations with 800×400 px $\sim 200 \times 100$ px to the SVF results from 1000×500 px images. It can be seen that the estimations with 800×400 , 600×300 , 500×250 , and 400×200 images only show small differences when compared with the largest size 1000×500 . And the R-squared (R^2) is between 0.983 and 0.992; Root Mean Squared Error (RMSE) is between 0.020 and 0.026. The 800×400 group has the closest estimation of 1000×500 size group is, followed by the 600×300 group. But even an image with 400×200 size can provide fair estimation results. Although the estimations from 300×150 and 200×100 images performed not as well as the others, they still provided estimations quite close to the SVF estimations from images with larger size, especially the 300×150 group, which had an RMSE of 0.055 and R^2 of 0.941. As a result, an image with 400×200 px in size can provide almost as good result as by large-sized images, and images with 300×150 in size can also provide fair results. Although the tests were performed with rectangular images, since rectangular and circular images are transformable, we could infer that circular fish-eye images

with a radius of 100 px (half the height of 400×200 image) could be enough for SVF estimation with our method.

The effect of image size on processing time is also tested. A comparison of processing time for different image sizes are shown in Fig. 12. The average processing time per image varies from 1.47s to a merely 0.08s for different image sizes. The processing time needed drops abruptly from 1000×500 px images to 200×100 px images, and images with a size of 500×250 px is able to provide preferable estimations with a speed of about 0.4s per image. Such efficiency enables large scale environmental factor survey opportunities.

3.2. Application example in four city centers

3.2.1. Survey sites

To demonstrate the application of the method proposed in this paper, the SVF in the metropolitan areas of four Chinese cities: Shanghai (31.2N, 121.5E), Xi'an (34.2N, 108.9E), Chongqing (29.5N, 106.5E), and Shenyang (41.8N, 123.4E) have been estimated. The average temperature and daily solar radiation in July (summer) and January (winter) for the four tested cities are listed in Table 1. The population densities of the administrative districts where the sample city centers lie in are also shown in Table 1. If the sample area covers more than one administrative districts, then an averaged population density of these districts is used. Shanghai is a global financial center and transport hub located on the eastern coast of China with a humid subtropical climate, and is known for its exponential urbanisation rate which has resulted in severe UHI effect [60]. It has the largest population density ($32,088/\text{km}^2$) in the four sample city centers. Chongqing is a major city in southwest China with a population of over 30 million

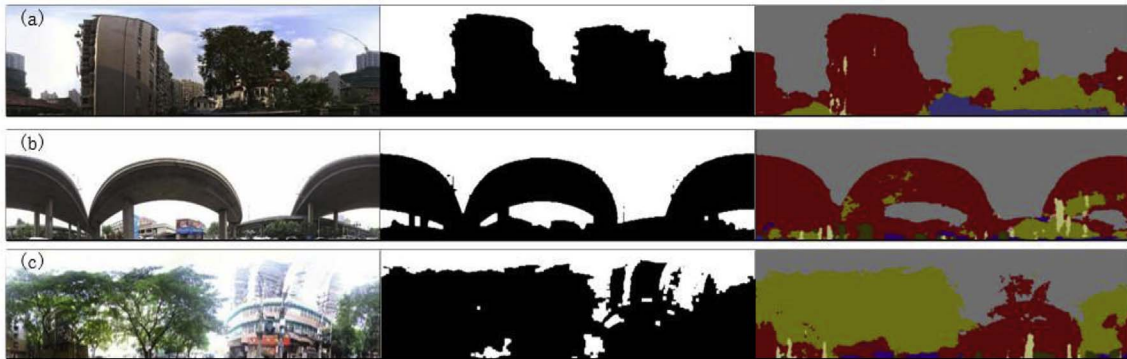


Fig. 10. Samples of sky region detection results (middle column), compared with SegNet [54] processed results (right column) for different difficult situations: (a) with blue sky and clouds; (b) with overhanging bridges; (c) an overexposed photo that has bad quality. (For interpretation of the references to color in this figure legend, the reader is referred to the Web version of this article.)

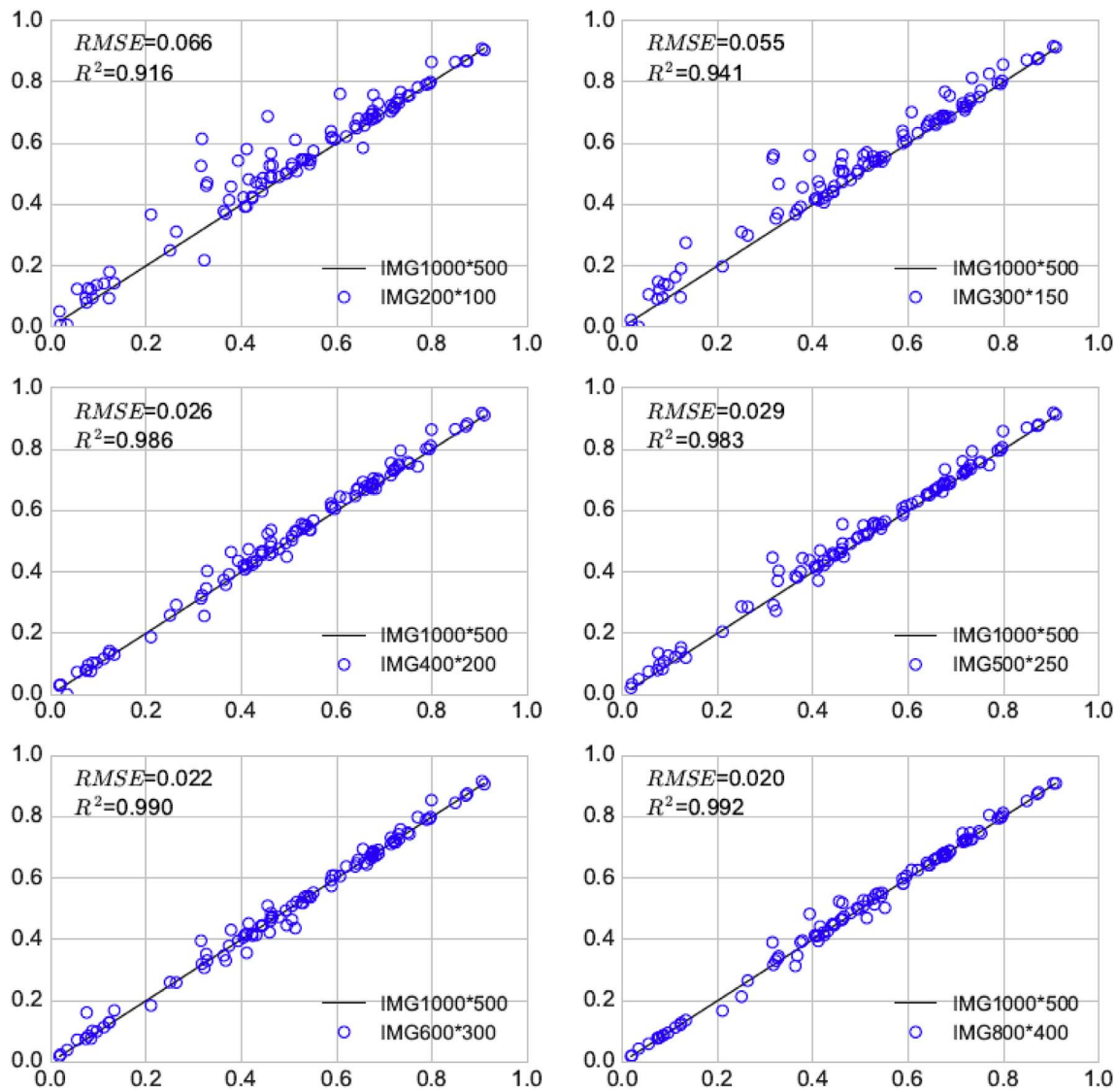


Fig. 11. RMSE and R^2 for selected sample images with different sizes when compared to panorama images with the size of 1000×500 px.

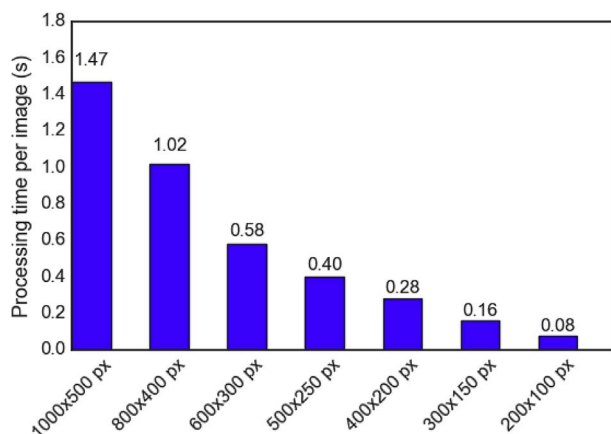


Fig. 12. Processing time per image for different image sizes.

and is also characterized by a humid subtropical climate. Xi'an is located in central China and characterized as a plain city. The surveyed areas for Chongqing and Xi'an are both located in their most populated districts with population densities of $28,239/\text{km}^2$ and $21,840/\text{km}^2$. Shenyang is the most populated city in the northeastern region of China

Table 1

Monthly average temperature, monthly average daily solar radiation, and estimated population density of the four sample areas.

Parameter	Shanghai	Chongqing	Xi'an	Shenyang
Climate classification	Humid subtropical	Humid subtropical	Humid subtropical	Humid continental
July Avg. Temperature ($^{\circ}\text{C}$)	27.5	28.4	26.7	25.7
July Avg. daily solar radiation (W/m^2)	4006	546	3392	4683
Jan. Avg. Temperature ($^{\circ}\text{C}$)	7.4	8.0	-0.4	-11.5
Jan. Avg. daily solar radiation (W/m^2)	2108	1847	2498	2341
Population density of the surveyed administrative district, 2015 ($/\text{km}^2$)	32,088	28,239	21,840	31,382

with extremely cold winters. The surveyed area for Shenyang has the second largest population density ($31,382/\text{km}^2$) among the four sample city centers.

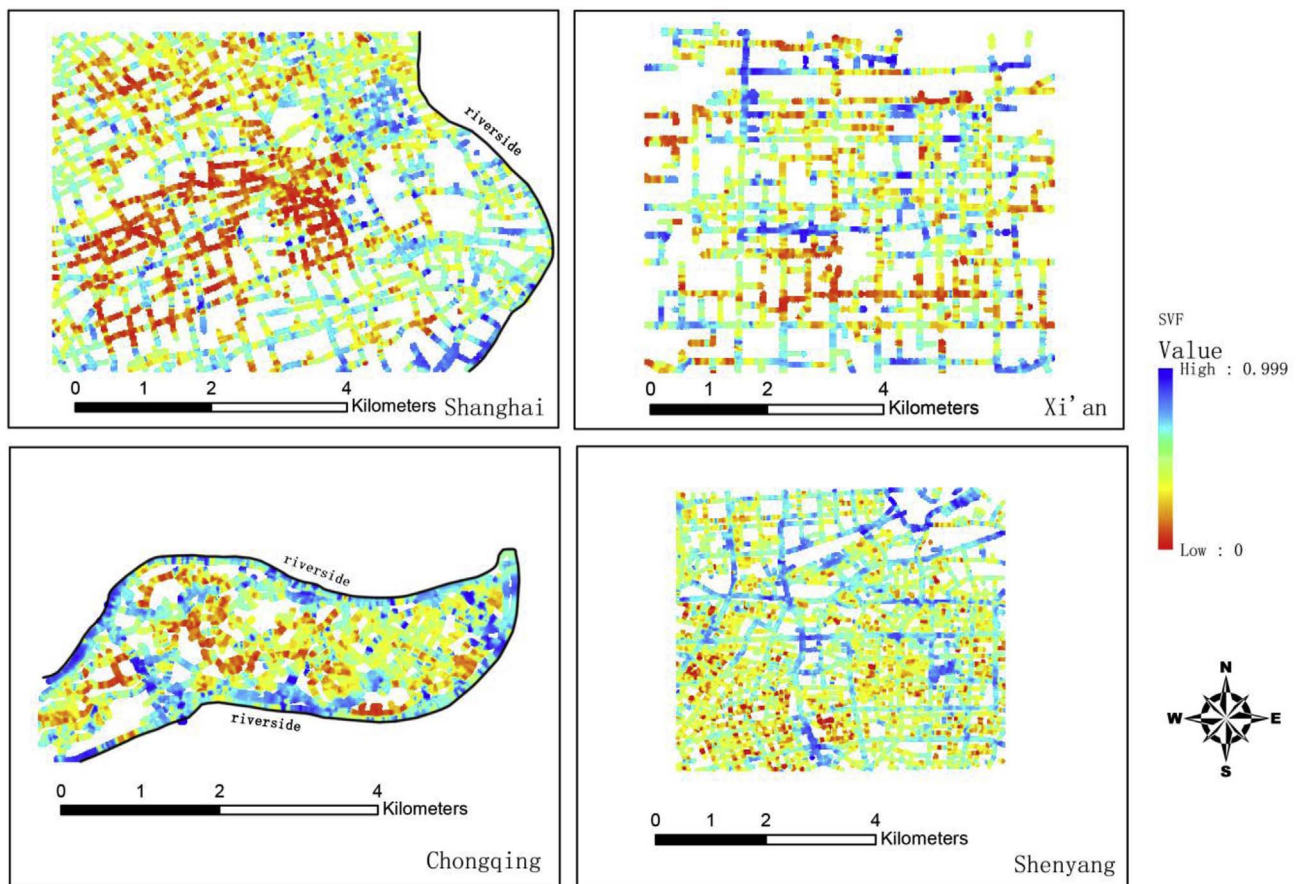


Fig. 13. The spatial patterns of SVF in the 4 sample city centers (Shanghai, Xi'an, Chongqing, Shenyang).

3.2.2. Current status of SVF in the sample city centers

Fig. 13 shows a contour map of SVF distribution in the 4 tested city centers. As shown, the distribution patterns of SVF vary significantly from city to city. It should be noted that even though the sampling points on road net are equally spaced, some of the main roads are two-way or four-way roads, which may increase the weight of such area because of the larger density of sampling points. So a contour map was interpolated with the obtained points using ArcMap's interpolation tool. The histograms of SVF distributions for each city are shown in Fig. 14. Shanghai has the lowest average SVF (0.43, standard deviation = 0.23) among the four cities, followed by Xi'an (mean = 0.47, standard deviation = 0.24) and Chongqing (mean = 0.50, standard deviation = 0.23). SVF in Xi'an and Chongqing shows a tendency of higher frequency in median SVF value and small frequency in both low and high SVF values, while Shanghai shows a slightly different pattern of higher frequency in low SVF. A large area in the central part of the surveyed area in Shanghai is obviously dominated by low SVF values (0–0.3). One reason is that it is the most developed cities in China and it has more skyscrapers; another reason is probably that it has more roadside vegetation. A unique feature of Chongqing center is the low SVF along the riverside area, because the city center is a peninsula surrounded by two rivers. Eliminating these river bank area, the average SVF in the investigated areas of Chongqing is 0.48 (standard deviation = 0.23). This value highly resembles the mean SVF of the central area of Xi'an, which might be due to similar urban planning strategies under similar climates. The mean SVF is largest (mean = 0.62, standard deviation = 0.15) in Shenyang. It should be noted that street view images obtained for the four tested city centers are taken in the leaf-on season and the effect of vegetation is negligible. Previous study has shown that SVF is positively related to both the nocturnal cooling and daytime solar energy gains. And as indicated in

literature [15], shading is a significant factor in regions with hot summer. This means the low SVF distribution in the city center might be beneficial to summer shading but may contribute to higher nighttime UHI intensity. The overall lower SVF in the northern city Shenyang is beneficial to solar access in winter, which complies with its main thermal demands as a northern city. Moreover, the SVF distribution in Shenyang's city center shows the smallest standard deviation, which implies the city's spatial pattern may involve less diversity compared to the other sample cities.

The above example demonstrates the method's successful application of capturing overall street canyon openness characteristics with the indicator SVF. This working process can be useful in future studies on outdoor thermal environment, urban planning, and urban renovation, since it can reveal precisely the current street canyon openness with all possible components such as vegetation in consideration. However, it should be noted that SVF also varies temporally because of city reconstruction and seasonal variation of foliage amounts. In occasions where street view images are not available, the developed sky segmentation method can also deal with on-site mobile obtained images accurately and efficiently. Moreover, future studies could also include the solar radiation estimation based on SVF mask. In conclusion, we see a vast opportunity of outdoor built environmental studies with this method, which could render better comprehensions of actual local outdoor environmental settings at a larger scale.

4. Conclusion

Sky view factor (SVF) is one of the most useful urban spatial indicators for radiation and thermal environmental assessment. Fish-eye photography has been widely applied in estimating SVF, and compared to obtaining SVF with 3D spatial datasets, this method is more

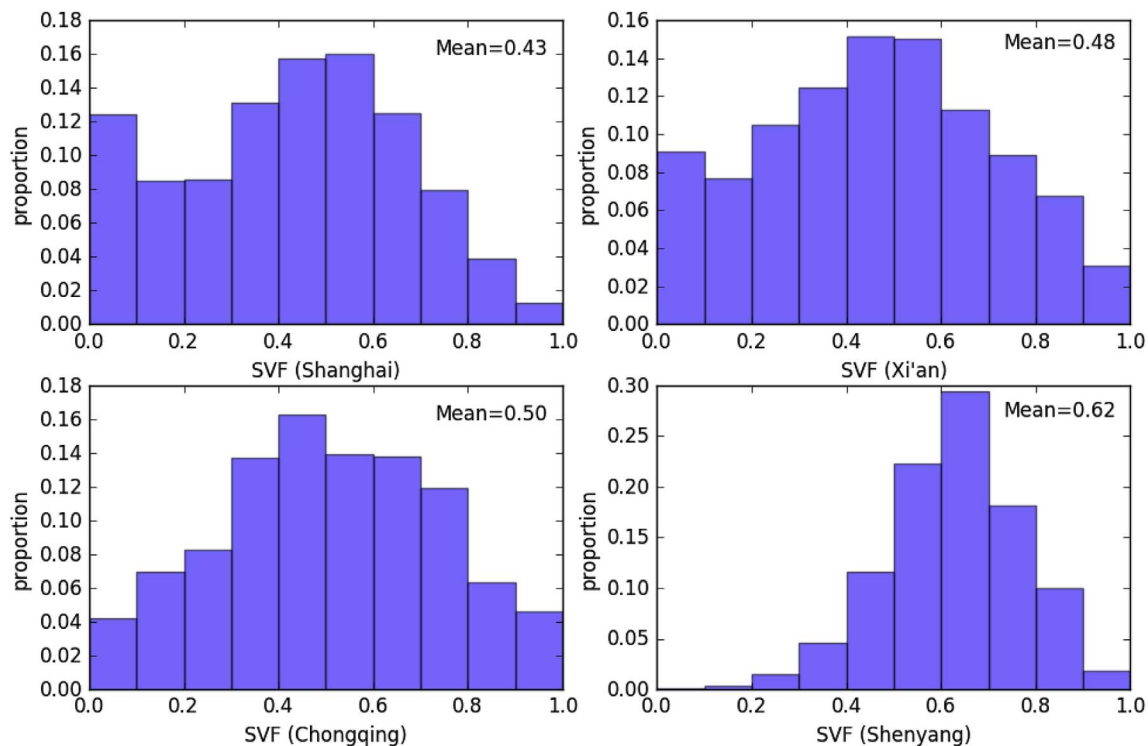


Fig. 14. Frequency distributions of SVF in the four tested city centers.

straightforward and convenient. But for a large continuous area or many points of interest, processing fish-eye photos may be labor intensive. This paper presents a workflow for estimating SVF from a large amount of street view images obtained at sampling points along city road network. A tool is developed with the Python programming language and the cross-platform open source computer vision library OpenCV to automatically estimate the SVF with street view images. Estimations with street view images were compared with the results with on-site fish-eye photos. Results show that the method can provide reliable estimations and preferable speed.

The proposed method was tested on estimating the SVF distributions in downtown centers of four densely populated cities in China. The procedure is handy and fast, and it is demonstrated to be able to reveal the contemporary status of SVF distribution in large scale built-environment. Overall, despite the similar population densities in the four tested cities, SVF distribution in the surveyed city centers show different patterns. The large scale survey could be helpful for urban planning and urban climate studies. One potential limitation of this method is the estimation results would be affected by seasonal variation of vegetation, this on the other hand may provide the opportunity to study the seasonal variation of intra-urban SVF. Another limitation is the coverage of survey sites is determined by street view image availability, and the streetview images are captured at about 2 m above ground, which is slightly different from the normally used pedestrian height (1.5 m). However, the image processing tool is so fast that on-site survey for the uncovered area can be completed within a short time. The developed tool can deal with even very small image sizes (e.g., 200 × 100 px) with fairly good estimation but much shorter time (17x faster) compared with large photos, making the process potential for real-time SVF estimation. This study explored the application of big data in faster investigation into large scale urban environment with high resolution, which may contribute to a more comprehended understanding in urban climate related issues.

Acknowledgments

This work is sponsored by National Science Foundation of China (No. 51478058, No. 51708054) and The 111 Project (No. B13041).

References

- [1] S. Achour-Younsi, F. Kharat, Outdoor thermal comfort: impact of the geometry of an urban street canyon in a Mediterranean subtropical climate – case study Tunis, Tunisia, *Procedia Soc. Behav. Sci.* 216 (2016) 689–700, <http://dx.doi.org/10.1016/j.sbspro.2015.12.062>.
- [2] L. Martinelli, A. Matzarakis, Influence of height/width proportions on the thermal comfort of courtyard typology for Italian climate zones, *Sustain. Cities Soc.* 29 (2017) 97–106, <http://dx.doi.org/10.1016/j.scs.2016.12.004>.
- [3] J.A. Rodríguez Algeciras, L. Gómez Consuegra, A. Matzarakis, Spatial-temporal study on the effects of urban street configurations on human thermal comfort in the world heritage city of Camagüey-Cuba, *Build. Environ.* 101 (2016) 85–101, <http://dx.doi.org/10.1016/j.buildenv.2016.02.026>.
- [4] A.S. Nouri, J.P. Costa, A. Matzarakis, Examining default urban-aspect-ratios and sky-view-factors to identify priorities for thermal-sensitive public space design in hot-summer Mediterranean climates: the Lisbon case, *Build. Environ.* (2017), <http://dx.doi.org/10.1016/j.buildenv.2017.10.027>.
- [5] L. Martinelli, T.P. Lin, A. Matzarakis, Assessment of the influence of daily shadings pattern on human thermal comfort and attendance in Rome during summer period, *Build. Environ.* 92 (2015) 30–38, <http://dx.doi.org/10.1016/j.buildenv.2015.04.013>.
- [6] T.P. Lin, A. Matzarakis, R.L. Hwang, Shading effect on long-term outdoor thermal comfort, *Build. Environ.* 45 (2010) 213–221, <http://dx.doi.org/10.1016/j.buildenv.2009.06.002>.
- [7] E.L. Krüger, F.O. Minella, F. Rasia, Impact of urban geometry on outdoor thermal comfort and air quality from field measurements in Curitiba, Brazil, *Build. Environ.* 46 (2011) 621–634, <http://dx.doi.org/10.1016/j.buildenv.2010.09.006>.
- [8] L. Chen, B. Yu, F. Yang, H. Mayer, Intra-urban differences of mean radiant temperature in different urban settings in Shanghai and implications for heat stress under heat waves: a GIS-based approach, *Energy Build.* 130 (2016) 829–842, <http://dx.doi.org/10.1016/j.enbuild.2016.09.014>.
- [9] T.R. Oke, Canyon geometry and the nocturnal urban heat-island - comparison of scale model and field observations, *J. Climatol.* 1 (1981) 237.
- [10] M.K. Svensson, Sky view factor analysis – implications for urban air temperature differences, *Meteorol. Appl.* 11 (2004) 201–211, <http://dx.doi.org/10.1017/S1350482704001288>.
- [11] F. Bourbia, H.B. Awbi, F. Bourbia, H.B. Awbi, Building cluster and shading in urban canyon for hot dry climate Part 2: shading simulations, *Renew. Energy* 29 (2004) 291–301, [http://dx.doi.org/10.1016/S0960-1481\(03\)00170-8](http://dx.doi.org/10.1016/S0960-1481(03)00170-8).
- [12] J. Yang, M.S. Wong, M. Menenti, J. Nichol, Study of the geometry effect on land

- surface temperature retrieval in urban environment, *ISPRS J. Photogrammetry Remote Sens.* 109 (2015) 77–87, <http://dx.doi.org/10.1016/j.isprsjprs.2015.09.001>.
- [13] D. Fröhlich, Development of a Microscale Model for the Thermal Environment in Complex Areas, Albert-Ludwigs-Universität Freiburg im Breisgau, 2016.
- [14] G.T. Johnson, I.D. Watson, The determination of view-factors in urban canyons, *J. Appl. Meteorol. Climatol.* 23 (1984) 329–335, [http://dx.doi.org/10.1175/1520-0450\(1984\)023<0329:TDOVFI>2.0.CO;2](http://dx.doi.org/10.1175/1520-0450(1984)023<0329:TDOVFI>2.0.CO;2).
- [15] I.D. Watson, G.T. Johnson, Graphical estimation of sky view-factors in urban environments, *J. Climatol.* 7 (1987) 193–197.
- [16] M.J. Brown, S. Grimmond, C. Ratti, Comparison of methodologies for computing sky view factor in urban environments, *Proc. 2001 Int. Symp. Environ. Hydraul.*, 2001, p. 6.
- [17] M. Taleghani, L. Kleerekoper, M. Tenpierik, A. Van Den Dobbels, Outdoor thermal comfort within five different urban forms in The Netherlands, *Build. Environ.* 83 (2015) 65–78, <http://dx.doi.org/10.1016/j.buildenv.2014.03.014>.
- [18] J. Yang, M.S. Wong, M. Menenti, J. Nichol, Modeling the effective emissivity of the urban canopy using sky view factor, *ISPRS J. Photogrammetry Remote Sens.* 105 (2015) 211–219, <http://dx.doi.org/10.1016/j.isprsjprs.2015.04.006>.
- [19] J. Yang, M.S. Wong, M. Menenti, J. Nichol, J. Voogt, E.S. Kravchenko, P.W. Chan, Development of an improved urban emissivity model based on sky view factor for retrieving effective emissivity and surface temperature over urban areas, *ISPRS J. Photogrammetry Remote Sens.* 122 (2016) 30–40, <http://dx.doi.org/10.1016/j.isprsjprs.2016.09.007>.
- [20] X. Yang, Y. Li, The impact of building density and building height heterogeneity on average urban albedo and street surface temperature, *Build. Environ.* 90 (2015) 146–156, <http://dx.doi.org/10.1016/j.buildenv.2015.03.037>.
- [21] F. Bourbia, H.B. Awbi, Building cluster and shading in urban canyon for hot dry climate Part 1: air and surface temperature measurements, *Renew. Energy* 29 (2004) 249–262, [http://dx.doi.org/10.1016/S0960-1481\(03\)00170-8](http://dx.doi.org/10.1016/S0960-1481(03)00170-8).
- [22] T.R. Oke, Canyon geometry and the nocturnal urban heat island: comparison of scale model and field observations, *J. Climatol.* 1 (1981) 237–254.
- [23] J. Unger, Connection between urban heat island and sky view factor approximated by a software tool on a 3D urban database, *Int. J. Environ. Pollut.* 36 (2009) 59, <http://dx.doi.org/10.1504/IJEP.2009.021817>.
- [24] A. Matzarakis, F. Rutz, H. Mayer, Modelling radiation fluxes in simple and complex environments: basics of the RayMan model, *Int. J. Biometeorol.* 54 (2010) 131–139, <http://dx.doi.org/10.1007/s00484-009-0261-0>.
- [25] J. Holst, H. Mayer, Impacts of street design parameters on human-biometeorological variables, *Meteorol. Z.* 20 (2011) 541–552, <http://dx.doi.org/10.1127/0941-2948/2011/0254>.
- [26] T.P. Lin, K.T. Tsai, R.L. Hwang, A. Matzarakis, Quantification of the effect of thermal indices and sky view factor on park attendance, *Landsc. Urban Plann.* 107 (2012) 137–146, <http://dx.doi.org/10.1016/j.landurbplan.2012.05.011>.
- [27] F. Bourbia, F. Boucheriba, Impact of street design on urban microclimate for semi arid climate (Constantine), *Renew. Energy* 35 (2010) 343–347, <http://dx.doi.org/10.1016/j.renene.2009.07.017>.
- [28] L. Chen, E. Ng, X. An, C. Ren, M. Lee, U. Wang, Z. He, Sky view factor analysis of street canyons and its implications for daytime intra-urban air temperature differentials in high-rise, high-density urban areas of Hong Kong: a GIS-based simulation approach, *Int. J. Climatol.* 32 (2012) 121–136, <http://dx.doi.org/10.1002/joc.2243>.
- [29] T. Gál, J. Unger, Urban Climate A new software tool for SVF calculations using building and tree-crown databases, *Urban Clim.* 10 (2014) 594–606, <http://dx.doi.org/10.1016/j.uclim.2014.05.004>.
- [30] L. Chapman, J.E. Thornes, A.V. Bradley, Sky-view factor approximation using GPS receivers, *Int. J. Climatol.* 22 (2002) 615–621, <http://dx.doi.org/10.1002/joc.649>.
- [31] L. Chapman, J.E. Thornes, Real-time sky-view factor calculation and approximation, *J. Atmos. Ocean. Technol.* 21 (2004) 730–741, [http://dx.doi.org/10.1175/1520-0426\(2004\)021<0730:RSFCAA>2.0.CO;2](http://dx.doi.org/10.1175/1520-0426(2004)021<0730:RSFCAA>2.0.CO;2).
- [32] A.V. Bradley, J.E. Thornes, L. Chapman, A method to assess the variation of urban canyon geometry from sky view factor transects, *Atmos. Sci. Lett.* 2 (2001), <http://dx.doi.org/10.1006/asle.2001.0031>.
- [33] L.C.L. Souza, D.S. Rodrigues, J.F.G. Mendes, Sky-view factors estimation using a 3D-gis extension, Eighth Int. IBPSA Conf., 2003, pp. 1227–1234.
- [34] A. Matzarakis, O. Matuschek, Sky view factor as a parameter in applied climatology - rapid estimation by the SkyHelios model, *Meteorol. Z.* 20 (2011) 39–45, <http://dx.doi.org/10.1127/0941-2948/2011/0499>.
- [35] O. Matuschek, A. Matzarakis, Berichte Des Meteorol., Estimation of Sky View Factor in Complex Environment as a Tool for Applied Climatology vol. 20, Institut Des Albert-Ludwigs-Universität Freiburg, 2010, pp. 534–539.
- [36] F. Lindberg, C.S.B. Grimmond, A. Gabey, B. Huang, C.W. Kent, T. Sun, N.E. Theeuwes, L. Järvi, H.C. Ward, I. Capel-Timm, Y. Chang, P. Jonsson, N. Krave, D. Liu, D. Meyer, K.F.G. Olofson, J. Tan, D. Wästberg, L. Xue, Z. Zhang, Urban Multi-scale Environmental Predictor (UMEP): an integrated tool for city-based climate services, *Environ. Model. Software* 99 (2018) 70–87, <http://dx.doi.org/10.1016/j.envsoft.2017.09.020>.
- [37] S. Park, S.E. Tuller, Advanced view factor analysis method for radiation exchange, *Int. J. Biometeorol.* 58 (2014) 161–178, <http://dx.doi.org/10.1007/s00484-013-0657-8>.
- [38] A.S. Nouri, D. Fröhlich, M.M. Silva, A. Matzarakis, The impact of Tipuana tipu species on local human thermal comfort thresholds in different urban canyon cases in Mediterranean climates: Lisbon, Portugal, *Atmosphere (Basel)* 9 (2018), <http://dx.doi.org/10.3390/atmos9010012>.
- [39] J. Liang, J. Gong, J. Sun, J. Liu, A customizable framework for computing sky view factor from large-scale 3D city models, *Energy Build.* 149 (2017) 38–44, <http://dx.doi.org/10.1016/j.enbuild.2017.05.024>.
- [40] B. Holmer, A simple operative method for determination of sky view factors in complex urban canyons from fisheye photographs, *Meteorol. Z.* (1992) 236–239.
- [41] A. Matzarakis, RayMan and SkyHelios model - two tools for urban climatology, Proc. MeetoolsVIII, 8. Fachtagung Des Ausschusses Umweltmeteorologie der Dtsch. Meteorol. Gesellschaft 5 (2012), pp. 1–6 <http://www.urbandclimate.net/matzarakis/pub2012.php>.
- [42] L. Chapman, J.E. Thornes, A.V. Bradley, Rapid determination of canyon geometry parameters for use in surface radiation budgets, *Theor. Appl. Climatol.* 69 (2001) 81–89, <http://dx.doi.org/10.1007/s007040170036>.
- [43] R. Carrasco-Hernandez, A.R.D. Smedley, A.R. Webb, Using urban canyon geometries obtained from Google Street View for atmospheric studies: potential applications in the calculation of street level total shortwave irradiances, *Energy Build.* 86 (2015) 340–348, <http://dx.doi.org/10.1016/j.enbuild.2014.10.001>.
- [44] J. Liang, J. Gong, J. Sun, J. Zhou, W. Li, Y. Li, J. Liu, S. Shen, Automatic sky view factor estimation from street view photographs - a big data approach, *Rem. Sens.* 9 (2017) 1–17, <http://dx.doi.org/10.3390/rs9050411>.
- [45] V. Badrinarayanan, A. Kendall, R. Cipolla, SegNet: a Deep Convolutional Encoder-decoder Architecture for Image Segmentation, (2015), pp. 1–14, <http://dx.doi.org/10.1109/TPAMI.2016.2644615>.
- [46] L. Yin, Z. Wang, Measuring visual enclosure for street walkability: using machine learning algorithms and Google Street View imagery, *Appl. Geogr.* 76 (2016) 147–153, <http://dx.doi.org/10.1016/j.apgeog.2016.09.024>.
- [47] L. Yin, Q. Cheng, Z. Wang, Z. Shao, “Big data” for pedestrian volume: exploring the use of Google Street View images for pedestrian counts, *Appl. Geogr.* 63 (2015) 337–345, <http://dx.doi.org/10.1016/j.apgeog.2015.07.010>.
- [48] Baidu Street View API, (n.d.). <http://lbsyun.baidu.com/index.php?title=static> (Accessed December 4, 2017).
- [49] Tencent Street View API, (n.d.). http://lbs.qq.com/panostatic_v1/index.html (Accessed December 4, 2017).
- [50] P. Angelo, Radiometric alignment and vignetting calibration, *Proc. Camera Calibration Methods Comput. Vis. Syst.*, 2007, pp. 1063–1082 <http://scholar.google.com/scholar?hl=en&btnG=Search&q=intitle:Radiometric+alignment+and+vignetting+calibration#1>.
- [51] A. Middel, J. Lukaszczuk, R. Maciejewski, Sky view factors from synthetic fisheye photos for thermal comfort routing—a case study in Phoenix, Arizona, *Urban Plan* 2 (2017) 19, <http://dx.doi.org/10.17645/up.v2i1.855>.
- [52] Y. Shen, Q. Wang, Sky region detection in a single image for autonomous ground robot navigation, *Int. J. Adv. Rob. Syst.* 10 (2013) 1–13, <http://dx.doi.org/10.5772/56884>.
- [53] Y. Li, Q. Miao, J. Song, Y. Quan, W. Li, Single image haze removal based on haze physical characteristics and adaptive sky region detection, *Neurocomputing* 182 (2016) 221–234, <http://dx.doi.org/10.1016/j.neucom.2015.12.032>.
- [54] V. Badrinarayanan, A. Handa, R. Cipolla, SegNet: a Deep Convolutional Encoder-decoder Architecture for Robust Semantic Pixel-Wise Labelling, (2015) <http://arxiv.org/abs/1505.07293>, Accessed date: 4 December 2017.
- [55] OpenCV library, (n.d.). <https://opencv.org/> (Accessed December 5, 2017).
- [56] Canny Edge Detector — OpenCV 2.4.13.4 documentation, (n.d.). https://docs.opencv.org/2.4/doc/tutorials/imgproc/imgtrans/canny_detector/canny_detector.html (Accessed December 7, 2017).
- [57] N. Laungrunthip, A.E. McKinnon, C.D. Churcher, K. Unsworth, ge-based detection of sky regions in images for solar exposure prediction, 2008 23rd Int. Conf. Image Vis. Comput. New Zealand, IVCNZ, 2008, <http://dx.doi.org/10.1109/IVCNZ.2008.4762101>.
- [58] K-Means Clustering in OpenCV — OpenCV 3.0.0-dev documentation, (n.d.). https://docs.opencv.org/3.0-beta/doc/py_tutorials/py_ml/py_kmeans/py_kmeans_opencv/py_kmeans_opencv.html (Accessed December 5, 2017).
- [59] D.G. Steyn, The calculation of view factors from fisheye-lens photographs: research note, *Atmos. Ocean* 18 (1980) 254–258, <http://dx.doi.org/10.1080/07055900.1980.9649091>.
- [60] F. Yang, S.S.Y. Lau, F. Qian, Summertime heat island intensities in three high-rise housing quarters in inner-city Shanghai China: building layout, density and greenery, *Build. Environ.* 45 (2010) 115–134, <http://dx.doi.org/10.1016/j.buildenv.2009.05.010>.